Insight into winter haze formation mechanisms based on aerosol hygroscopicity and effective density measurements

Yuanyuan Xie[1], Xingnan Ye[1,2]*, Zhen Ma[1], Ye Tao[1], Ruyu Wang[1], Ci Zhang[1], Xin Yang[1,2], Jianmin Chen[1,2*], Hong Chen[1]

[1]Shanghai Key Laboratory of Atmospheric Particle Pollution and Prevention (LAP[3]), Department of Environmental Science and Engineering, Fudan University, Shanghai 200433, China.

[2] Institute of Atmospheric Sciences, Fudan University, Shanghai 200433, China.

*Correspondence to: Xingnan Ye (yexingnan@fudan.edu.cn), Jianmin Chen (jmchen@fudan.edu.cn).

Abstract: We characterize a representative particulate matter (PM) episode that occurred in Shanghai during winter 2014. Particle size distribution, hygroscopicity, effective density, and single particle mass spectrometry were determined online, along with offline analysis of water-soluble inorganic ions. The mass ratio of SNA/$PM_{1.0}$ (sulfate, nitrate, and ammonium) fluctuated slightly around 0.28, suggesting that both secondary inorganic compounds and carbonaceous aerosols contributed substantially to the haze formation, regardless of pollution level. Nitrate was the most abundant ionic species during hazy periods, indicating that NO_x contributed more to haze formation in Shanghai than did SO_2. During the representative PM episode, the calculated PM was always consistent with the measured $PM_{1.0}$, indicating

that the enhanced pollution level was attributable to the elevated number of larger particles. The number fraction of the near-hydrophobic group increased as the PM episode developed, indicating the accumulation of local emissions. Three “banana-shaped” particle evolutions were consistent with the rapid increase of $PM_{1.0}$ mass loading, indicating that the rapid size growth by the condensation of condensable materials was responsible for the severe haze formation. Both hygroscopicity and effective density of the particles increased considerably with growing particle size during the banana-shaped evolutions, indicating that the secondary transformation of NO_x and SO_2 was one of the most important contributors to the particle growth. Our results suggest that the accumulation of gas-phase and particulate pollutants under stagnant meteorological conditions and subsequent rapid particle growth by secondary processes, were primarily responsible for the haze pollution in Shanghai during wintertime.

Keywords: air pollution; size distribution; hygroscopic growth; secondary process; Shanghai.

1. Introduction

Atmospheric aerosol has significant influences on radiation balance and climate forcing of the atmosphere (Wang et al., 2011;Wang et al., 2014c;Wu et al., 2016a;IPCC, 2013). Also, atmospheric aerosol has s strong impacts on visibility (Yang et al., 2012;Lin et al., 2014;Xiao et al., 2014) and public health (Heal et al., 2012). Recent studies found that short-term exposure to haze pollution could cause airway inflammation and aggravate respiratory symptoms in chronic obstructive pulmonary disease

patients (Wu et al., 2016b;Guan et al., 2016).

With the huge achievements in economic development and rapid urbanization over the past 30 years, particulate pollution has become a major environmental concern in China. The most severe haze event that occurred in the first quarter of 2013, spread over 1.6 million km^2 (Wang et al., 2014a). This event motivated the release of the Action Plan on Prevention and Control of Air Pollution with the goal of reducing $PM_{2.5}$ (particulate matter smaller than 2.5 μm in aerodynamic diameter) concentration by 15–25% in 2017 against 2012 in three major city clusters (http://english.mep.gov.cn/News_service/infocus/201309/t20130924_260707.htm). In order to reduce the $PM_{2.5}$ concentration, extensive studies have been conducted to investigate the sources and formation mechanisms of haze pollution in recent years (Ye et al., 2011;Sun et al., 2016;Qiao et al., 2016;Hu et al., 2016;Li et al., 2016;Guo et al., 2014;Zheng et al., 2015;Guo et al., 2013;Wang et al., 2016;Peng et al., 2016). However, the haze formation mechanisms and source appointment of fine particles remain uncertain.

Guo et al. (2013) summarized historical reports from 2000 to 2008 in Beijing and found that the origins of urban fine particles varied in different seasons: the contribution of primary emissions is comparable to that of secondary formation during winter heating periods whereas secondarily produced aerosols dominate the fine PM sources in other seasons. As an important type of primary emissions in urban area, black carbon (BC) is primarily from incomplete fossil fuel combustion. Light absorption of

BC aerosols is increased after atmospheric aging by coating with secondary materials and restructuring (Khalizov et al., 2009). Due to cooling effect at the surface and warming effect aloft, the enhanced light absorption and scattering by aged BC particles stabilize the atmosphere, hindering vertical transport of gaseous and particulate pollutants (Wang et al., 2013). BC aging occurs much more efficiently in the presence of highly elevated gaseous aerosol precursors so that light absorption increases by a factor of 2.4 within 4.6 h under highly polluted conditions in Beijing, significantly exacerbating pollution accumulation and strongly contributing to severe haze formation (Peng et al., 2016).

Due to the implement of several effective regulatory policies, the increasing trend of primary emissions has been under control since the 11^{th} five-year period. A growing number of studies suggested that secondary production was the major contributor to the haze events in recent years (Shi et al., 2014;Zhao et al., 2013;Zhang et al., 2015a;Huang et al., 2014), in contrast with the fact that primary emissions were of great importance in some haze events (Niu et al., 2016). Guo et al. (2014) reported that the development of PM episodes in Beijing was characterized by efficient nucleation and continuous particle growth over an extend period dominated by local secondary formation. They attributed the continuous growth of particle size and constant accumulation of particle mass concentration to the highly elevated concentrations of gaseous precursors such as NO_x, SO_2, and volatile organic compounds (VOCs), while the contribution from primary emissions and regional transport was negligible. However, the role of regional transport of $PM_{2.5}$ in haze formation remains controversial (Li et al., 2015;Zhang et al., 2015b).

The most important advances in the understanding of urban PM formation were reviewed by Zhang et al. (2015c). The concentrations of SO_2, NO_x, and anthropogenic source VOCs in Beijing and other cities of the developing world are significantly higher than those in the urban areas of developed countries, resulting in large secondary production of sulfate, nitrate, and SOA. Synergetic effects among various organic and inorganic compounds may exist under highly polluted conditions, indicating different PM formation rates between developing and developed urban regions. Indeed, a large enhancement of particulate sulfate was typically observed during regional haze events in China (Chen et al., 2016;Wang et al., 2015;Fu et al., 2008;Xie et al., 2015). Currently, the highly elevated sulfate concentration during haze events cannot be fully explained by model simulations (Wang et al., 2014b;Chen et al., 2016). Recently, a significant breakthrough made by Wang et al. (2016) has provided a reasonable explanation about the high level of sulfate during haze events. It was revealed by their laboratory experiments that the aqueous oxidation of SO_2 by NO_2 proceeds more efficiently with the increase of NO_2 concentration whereas the reaction is suppressed in acid conditions, because acid effect reduces the solubility of SO_2 and reaction rate. The enhanced sulfate formation during severe haze periods in Beijing was attributable to aqueous oxidation of SO_2 by NO_2 on hygroscopic fine particles under conditions of elevated RH and the concentrations of NH_3 and NO_2, as confirmed by the comparable SO_2 uptake coefficients for sulfate formation from field and laboratory results.

The hygroscopic properties of ambient particles vary significantly depending on the origin of the air

masses and the atmospheric aging process. In urban air, the population of near-hydrophobic particles can be assumed to consist largely of freshly emitted combustion particles containing high mass fractions of soot and water-insoluble organic compounds (Swietlicki et al., 2008;Massling et al., 2009). In contrast, secondary sulfate or nitrate aged particles are more-hygroscopic, and their relative abundance is primarily responsible for the hygroscopic growth of ambient particles at elevated RH (Topping et al., 2005;Aggarwal et al., 2007;Gysel et al., 2007). Thus, hygroscopicity can serve as a tracer of source origins, mixing state, and aging mechanisms of ambient particles. For example, the temporal variation of aerosol hygroscopicity has thrown some new light on haze formation mechanisms in Beijing and Shanghai (Ye et al., 2011;Guo et al., 2014).

Density is one of the most important physicochemical properties for atmospheric aerosols. Effective density has served as a tracer for new particle formation and for the aging process in previous studies (Yin et al., 2015;Guo et al., 2014). The ambient particles in urban areas are mostly complex mixtures of elemental carbon (EC), organics (OC), and secondary inorganic aerosols (SIA) (Hu et al., 2012). The effective density of nascent traffic particles varies from approximately 0.9 g cm^{-3} to below 0.4 g cm^{-3}, decreasing with the increase of particle size, because there are more voids between primary particles in relatively larger aggregates (Momenimovahed and Olfert, 2015). The effective density of OC is in between those of EC and SIA, and varies with source. The effective density of combustion particles increases by filling the voids in the agglomerate particles with condensed semi-volatile materials, or by

restructuring agglomerates with hygroscopic SIA (Momenimovahed and Olfert, 2015;Zhang et al., 2008).

In this study, a combined HTDMA-APM system was used to investigate the variations of hygroscopicity and effective density of submicrometer aerosols during winter 2014 in urban Shanghai. In addition, cascade impactor samples were collected and temporal variations of particle composition were determined by a single particle mass spectrometry, which provided further insight into the hygroscopicity and density variations. The primary objectives of this study were to investigate the particle growth mechanisms and to identify the contribution of local emissions during the winter haze events.

2. Experimental

2.1. Sampling site

The measurements of particle hygroscopicity and effective density were conducted from December 21, 2014 to January 13, 2015 at the Department of Environmental Science and Engineering in the main campus of Fudan University (31.30°N, 121.5°E). It can be considered as a representative urban site for Shanghai. There are many dwelling quarters and commercial blocks in surrounding area. About 400 m away from the measurement site, there is the Middle Ring Line, one of the busiest elevated roads in the city.

2.2 Measurements of air quality index and ground meteorological parameters

At a supersite about 100 m away from the Environmental Building, $PM_{1.0}$ was monitored using a

Thermo Scientific™ 5030 SHARP monitor. Trace gas pollutants were monitored using Thermo Scientific™ i-series gas analyzers (43i for SO_2, 49i for O_3, 42i for $NO/NO_2/NO_x$), and meteorological data were monitored using an automatic meteorological station (Model CAWS600, Huayun Inc., China) (Yin et al., 2015). The datas of $PM_{2.5}$, PM_{10}, and CO were released by the Shanghai Environmental Monitoring Center. The height of the Planet Boundary Layer (PBL) was computed online using the NCEP Global Data Assimilation System (GDAS) model (http://ready.arl.noaa.gov/READYamet.php).

2.3. HTDMA-APM system

Particle size distribution, hygroscopic growth factor (GF), and effective density were measured using a custom-built HTDMA-APM system (Figure 1). The custom-built HTDMA (Hygroscopic Tandem Differential Mobility Analyzers) mainly consist of two long DMAs (3081L, TSI Inc.), a humidifier (PD-50T-12MSS, Perma Pure Inc.) and a Condensation Particle Counter (CPC, Model 3771, TSI Inc.). A detailed description of the HTDMA is available in Ye et al. (2009). In this observation, particle number size distribution in the range of 14–600 nm and hygroscopic growth at 83% RH for particles with dry diameters of 40, 100, 220, 300, 350, and 400 nm were determined by HTDMA in turn. The determination of effective density by DMA-APM was described previously (Yin et al., 2015;Pagels et al., 2009). Briefly, a combined system consisting of a compact Aerosol Particle Mass Analyzer (APM, Model 3601, Kanomax Inc.) and a CPC (Model 3775, TSI Inc.) was connected to the sample tubing through a 3-way electrical switch behind the upstream DMA (DMA1). The APM comprises two coaxial cylindrical

electrodes rotating at the same angular velocity. Charged aerosol particles of a certain diameter sized by DMA1 are axially fed into the annular gap between the electrodes and experienced an outward centrifugal force from the particle rotating and an inward electrostatic force from the high-voltage field between the electrodes. Particles pass through the APM and are sent to the CPC when the two forces are balanced. The mass of particles that pass through the APM is determined by the rotation rate and the applied voltage. Effective densities for dry diameters of 40, 100, 220, and 300 nm were determined by the method of DMA-APM in this study. The HTDMA-APM was operated alternatively in HTDMA mode and then DMA-APM mode, for every 40 min.

Before the field observation, the HTDMA-APM was calibrated using 40–450 nm NIST-Traceable PSL particles and ammonium sulfate. The measured HTDMA data were inversed with the $TDMA_{inv}$ algorithm to obtain the actual GF distribution. This is because the raw data are only a skewed and smoothed integral transform of the actual growth factor probability density function (GF-PDF) (Gysel et al., 2009). The hygroscopicity parameter κ was derived from the GF data after inversion with the $TDMA_{inv}$ algorithm according to the κ-Köhler theory (Petters and Kreidenweis, 2007).

2.4. SPAMS

A Single Particle Aerosol Mass Spectrometry (SPAMS, Hexin Analytical Instrument Co., Ltd., China) installed in the same room with the HTDMA-APM system was used to obtain the chemical and size information of individual particles in the range of 0.2-2 μm. Detailed information on SPAMS is available

in Li et al. (2011). Briefly, ambient particles are drawn into a vacuum chamber through an aerodynamic focusing lens and accelerated to a size-dependent terminal velocity. Sized particles are desorbed and ionized by the pulsed desorption/ionization laser (Q-switched Nd: YAG, λ=266 nm) at the ion source region. Both positive and negative mass spectra for a single particle are recorded by a bipolar time-of-flight spectrometer. The single particle information was imported into YAADA (version 2.11, www.yaada.org). Based on the similarities of the mass-to-charge ratio and peak intensity, particles were classified using the ART-2a method.

2.5. Ion chromatography

Cascade impactor aerosol samples for offline analysis were collected at the roof platform of the Environmental Building using a 10-stage MOUDI sampler (Micro-Orifice Uniform Deposit Impactor, Model 110-NR, MSP Corp., USA). Detailed description of the sampling, pretreatment, chemical analysis, and quality control of this system is available in Tao et al. (2016). Briefly, cascade impactor samples were collected every 24 h using the PALL7204 quartz filter as the collection substrate. Each filter was weighted with a BP211D electronic balance at 25±1°C and 40±2%RH. The water extract of each sample was analyzed using an Ion Chromatograph (Metrohm 883 basic IC plus, Switzerland) equipped with a third-party column heater (CT-100, Agela Corp., China). Seven anions (F^-, Cl^-, NO_2^-, Br^-, NO_3^-, SO_4^{2-} and PO_4^{3-}) were resolved using a Metrosep A Supp 5-250/4.0 column at 35°C with an eluent of 3.2 mmol L^{-1} Na_2CO_3 + 1.0 mmol L^{-1} $NaHCO_3$. Six cations (Li^+, Na^+, NH_4^+, K^+, Ca^{2+}, and Mg^{2+}) were separated by a Metrosep

C4-250/4.0 column at 30°C with an eluent of 1.7 mmol L^{-1} HNO_3 + 0.7 mmol L^{-1} 2,6-pyridine dicarboxylic acid.

3. Results and discussion

3.1. Periodic cycle of PM episodes during the observation period

Figure 2 shows the temporal variations of PM mass loading during the winter observation (December 21, 2014 to January 13, 2015). The official data of $PM_{2.5}$ and PM_{10} were blank on some clean days. Meteorologically, our measurement was deployed in a typical winter period. The average concentrations of $PM_{1.0}$, $PM_{2.5}$, and PM_{10} were 57 ± 37, 87 ± 67, and 129 ±78 μg m^{-3}, respectively. About 62% of hourly averaged $PM_{2.5}$ concentrations exceeded 75 μg m^{-3} of the Chinese Grade II guideline (GB 3095-2012), indicating heavy particle pollution in Shanghai during wintertime. The PM episodes exhibited a clear periodic cycle of ~5 days. A similar feature was previously observed in Beijing (Guo et al., 2014). At the beginning of each cycle, the $PM_{1.0}$ level was below 35 μg m^{-3}. Generally, the difference between the concentrations of $PM_{1.0}$ and $PM_{2.5}$ during clean days was less significant than that in haze periods. Occasionally the measured $PM_{2.5}$ concentrations were larger than those of PM_{10}, possibly due to system error. However, the particle mass concentration began to increase in the next few days, with $PM_{1.0}$ and $PM_{2.5}$ peaking at over 100 and 200 μg m^{-3}, respectively. During the end of each PM episode, the change in weather conditions played a key role in the decrease of particle concentration. As shown in Figure S1,

198 the prevailing winds on haze days were from the northwest. The prevailing winds during two clean periods
199 (December 25-27 and January 12-14) were northeasterly, bringing clean air mass from East China Sea.
200 Two cold fronts from the north swept Shanghai on December 31 and January 6, bringing gale and lower
201 temperature which favored the dispersion of atmospheric pollutants.

202 **3.2 Contributions of secondary inorganic aerosols to $PM_{1.0}$ mass loading**

203 Figure 3 illustrates the daily concentrations of sulfate, nitrate, and ammonium as a function of $PM_{1.0}$
204 mass loading. In general, the sum of concentrations of sulfate, nitrate, and ammonium (SNA) increased
205 linearly as the $PM_{1.0}$ mass loading increased. It is noticeable that the $SNA/PM_{1.0}$ ratio slightly fluctuated
206 around 0.28, regardless of the pollution level. Because soil dust and sea salt made a negligible contribution
207 to the fine particle mass concentration in this study, the almost constant ratio of $SNA/PM_{1.0}$ indicates that
208 SNA and carbonaceous aerosols (including soot and organic matter) synchronously increased during the
209 haze events. As the $PM_{1.0}$ concentration increased, the concentration of nitrate increased more rapidly
210 than sulfate so that it became the most abundant ionic species at $PM_{1.0} > 40$ μg m^{-3}. This finding indicates
211 that NO_x contributed more to haze formation in Shanghai compared to SO_2. Generally, the visibility
212 decreased with the increase in PM concentration, indicating photochemical activity began to weaken as
213 the development of haze events. The large increase in nitrate concentration may be attributable to
214 heterogeneous reaction on the preexisting particles. Nitrate formation is highly dependent on the surface
215 area of preexisting particles and is favored under NH_3-rich conditions (Chu et al., 2016). In contrast, Han

et al. (2016) reported that the mass ratio of nitrate to sulfate decreased with the increase of $PM_{2.5}$ level and that the sources of sulfate contributed more to the haze formation in Beijing than mobile sources. This finding suggests that the haze formation mechanism in Shanghai is likely different from that in Beijing. VOCs and NO_x are exclusively from local emissions whereas regional transport is a big source of SO_2 under stagnant atmosphere, due to different atmospheric lifetimes among SO_2, NO_x, and VOCs (Guo et al., 2014). Considering the relatively smaller contribution of sulfate, our results reveal that the accumulation and secondary transformation of local emissions likely played a dominant role in this haze formation.

3.3 Aerosol hygroscopicity and effective density during the observation period

Figure 4a displays a box chart of the mean hygroscopicity of each hygroscopic growth factor distribution for different sizes. Considering all of the growth factor distributions collectively, the hygroscopicity parameter κ increased with increase of the dry diameter, with a mean κ of 0.161 at 40 nm and 0.338 at 300 nm. Assuming a two-component system of a model salt (ammonium sulfate, $\kappa_m = 0.53$) and an insoluble species ($\kappa = 0$), the volume fraction of hygroscopic species (ε) can be obtained based on the Zdanovsldi-Stokes-Robinson (ZSR) mixing rule. The average ε was 0.3 for 40 nm particles, suggesting that the primary particles or initial growth of freshly generated particles were dominated by non-hygroscopic species. In contrast, the 300 nm particles were extremely aged, with more-hygroscopic species.

Generally, HTDMAs measure dry particles smaller than 300 nm due to technical limitations, and it is common that particle hygroscopicity increases with the increase of particle size (Liu et al., 2014;Swietlicki et al., 2008). The increase of particle hygroscopicity with particle size was attributed to the addition of more-hygroscopic SNA (Swietlicki et al., 2008;Ye et al., 2010). The very few measurements for dry particles larger than 300 nm showed different size dependencies. Gasparini et al. (2006) reported that particle hygroscopicity first increased and then decreased with the increase of particle size, peaking at the diameter of 300 nm. In contrast, Wu et al. (2016c) reported that particle hygroscopicity increased with particle diameter in the range of 35-350 nm. In this study, the determination size range was extended to 400 nm and the mean κs of 300, 350, and 400 nm particles were nearly equal. We attribute the different size dependencies of hygroscopicity among various measurement sites to the total emissions of SO_2 and NO_x, gas precursors of hygroscopic sulfate and nitrate. It is noticeable that the 5^{th} percentile hygroscopicity decreased for dry diameter larger than 300 nm, likely due to the presence of the smallest dust particles (Gasparini et al., 2006). The variability of hygroscopicity parameter κ was much greater for 40 nm particles. The particle population with $\kappa < 0.1$ was attributed to fresh traffic particles (Ye et al., 2013). The considerable percentile of $\kappa < 0.1$ indicates that the 40 nm particle population was sometimes dominated by near-hydrophobic particles.

Figure 4b displays a box chart of median effective density for different particle sizes. The median effective density varied in the narrow range of ρ_{eff} = 1.35–1.41 g cm^{-3} for 40–300 nm particle population.

The size dependency of particle effective density varied in the literature. Hu et al. (2012) and Yin et al. (2015) reported that effective density of the particles increased as particle size increased while a opposite trend was observed by Geller et al. (2006) and Spencer et al. (2007). The different trends were attributable to the variable fraction of lower density mode particles (ρ_{eff} < 1.0 g cm^{-3}). The densities of the secondarily produced $(NH_4)_2SO_4$, NH_4HSO_4, and NH_4NO_3 are ~1.75 g cm^{-3}. The effective density of organic aerosols varies mostly in the range of 1.2-1.6 g cm^{-3}, depending on their source origins (Malloy et al., 2009;Turpin and Lim, 2001;Dinar et al., 2006). The lower density particles with ρ_{eff} < 1.0 g cm^{-3} were attributable to fresh or partially aged traffic-related particles, because the number fraction of the lower density group in urban area was found to be consistent with the concentration of NO (indicator of traffic) (Levy et al., 2013;Rissler et al., 2014). Although the dominant accumulation mode particles have an effective density greater than Aitken mode ones, the presence of a lower effective density group associated with traffic emissions might decrease the mean effective density to a value lower than that of Aitken mode particles (Levy et al., 2014). Yin et al. (2015) reported that effective density distributions were dominated by a single peak in the previous observation. In contrast, a lower density peak below1.0 g cm^{-3} was often present in this observation, decreasing the mean effective density of externally mixed aerosols.

3.4 Characteristics of a representative PM episode

As shown in Figure 2, the PM episode from January 7 to 12 was a representative case of severe haze formation and elimination processes. It can be divided into clean (January 7), transition (January 8), haze

(January 9–11), and post-haze (January 12) periods. During the transition from the clean period to haze period (January 7 to 8), both $PM_{1.0}$ and $PM_{2.5}$ concentrations increased slightly, with an average $PM_{1.0}/PM_{2.5}$ ratio of 0.65. A sharp increase in $PM_{2.5}$ (of 125 μg m^{-3}) was observed from 6:00 to 12:00 local time on the morning of January 9. During the haze period, the concentration of $PM_{2.5}$ exceeded 115 μg m^{-3} (medially polluted level, HJ633-2012) for 63 h. On January 11, the hourly $PM_{2.5}$ concentration exceeded 250 μg m^{-3}, corresponding to the severely polluted level.

Figure 5 displays the temporal profile of particle size distribution, along with the measured $PM_{1.0}$ concentration during the representative PM episode. The calculated PM concentrations (PM_{cal}) were obtained based on the particle size distribution and average effective density of 1.39 g m^{-3} in the range of 14–600 nm measured in this study. It is noticeable that the temporal trends in mass concentrations of PM_{cal} and $PM_{1.0}$ are highly consistent. In contrast to the fact that particle size distribution was dominated by nanoparticles during the clean period, the burst of Aitken mode particles and subsequent continuous growth to approximately 200 nm in diameter was observed three times during the haze period, indicating that the presence of numerous larger particles is likely responsible for the severe particle pollution (Guo et al., 2014). The importance of larger particles in haze formation is also illustrated by the contour plot of the particle volume size distribution. The difference of particle number concentration between transition and haze periods was less significant, whereas the volume concentration increased considerably during the haze period. This feature clearly demonstrates that the haze formation was closely correlated with

particle growth and elevated number of larger particles.

Interestingly, the particle mass concentration was sensitive to variations of wind speed and planetary boundary layer (PBL). During the transition and haze periods, the wind speed decreased considerably with insignificant change in prevailing wind (Figure S1). This finding indicates that outside transportation became less and less significant. It is noteworthy that the temporal evolution of the particle mass concentration was inversely correlated with the PBL height. The decreasing PBL provided a stagnant atmosphere that favored the accumulation of local emissions. This finding reveals that the severe haze pollution was likely triggered by the adverse meteorological conditions. The impact of decreasing PBL height on haze formation can also be evidenced by the variations of trace gaseous species (Figure S2). During the PM episode, the concentrations of NO_2, SO_2, and CO displayed variation trends similar to that of the particle concentration. The fluctuations of trace gas concentrations were caused by primary emission and secondary processes. Noticeably, the concentration of NO increased dramatically in rush hours during the haze period, whereas it fluctuated slightly during the clean period; indicating that local emissions were easily accumulated under stagnant atmosphere. In addition, the maximum concentration of O_3 remained considerably higher during daytime, whereas it decreased significantly at night. The most plausible explanation is that O_3 was consumed rapidly by the accumulated trace gases, such as NO_x, and VOCs.

3.5 Variations of hygroscopicity and effective density during the PM episode

306 Figure 6 shows the averaged hygroscopicity and effective density for different pollution periods of the
307 PM episode. Regardless of the pollution period, the nearly-hydrophobic particles were externally mixed
308 with some hygroscopic particles. During the clean period, the more-hygroscopic particles dominated the
309 40 nm particle population, indicating that the near-hydrophobic primary particles were rapidly dispersed
310 due to atmospheric dilution. The number fraction of the near-hydrophobic group for different sizes
311 increased as the PM episode developed, indicative of the increasing accumulation of local emissions.
312 Notably, the increase of the near-hydrophobic particles with the evolution of the PM episode become less
313 significant as particle size increased, indicating that primary emission exerted a more significant impact
314 on smaller particles than on larger ones. The median diameter of nascent traffic particles from various
315 gasoline sources ranged between 55 and 73 nm with an average of 65 nm (Momenimovahed and Olfert,
316 2015). Therefore, the number fraction of the near-hydrophobic particles larger than 200 nm is not sensitive
317 to the accumulation of traffic emissions.

318 Interestingly, the variations of particle effective density for different sizes are in good agreement with
319 the hygroscopicity. The dominant peak of effective density distribution appeared at ρ_{eff} = ~1.5 g cm^{-3} for
320 40 nm particles in the clean period, indicating that they are highly aged with hygroscopic inorganic salts
321 (Yin et al., 2015). As the episode developed, the mean density shifted to lower values, indicating the
322 increasing contribution of lower density carbonaceous materials. The averaged density distribution was
323 broadened as the episode developed, suggesting that it could be deconvolved into two groups and that the

number fraction of the low-density group increased. This finding revealed that the lower density particles are less hygroscopic whereas the larger density group corresponds to the more-hygroscopic one. In addition, the variations of hygroscopicity and effective density coincided with the evolution of PBL height, indicating that the increasing accumulation of local emissions due to adverse atmospheric conditions is likely responsible for the enhancement of those near-hydrophobic and lower density particles.

Figure 7 displays the temporal profiles for contributions of EC (including bare EC and OC-coated EC), OC, sulfate, and nitrate determined by SPAMS. Obviously, the relative contribution of nitrate increased as the episode developed. In contrast, the relative contribution of sulfate displayed an opposite trend. This feature is comparable with the aforementioned results of SNA, thus further highlighting the important role of nitrate in haze formation in Shanghai. The number fraction of EC particles generally increased during the haze period, peaking at midnight on January 9 and 10. It should be pointed out that the measured number fraction possibly underestimated the contribution of EC particles because the dominant size range of fresh traffic particles is below the detection limit of SPAMS (0.2–2.0 μm). This finding provides good support for the increase of near-hydrophobic and lower density particles as the episode developed. Niu et al. (2016) reported that the number ratio of secondary particles to soot in haze samples was higher than that collected in the clean days in Beijing. Our finding is comparable to their results. In contrast, the number fraction of pure OC decreased during the pollution event. The possible explanation is that the condensation of organic matter was favored on the large amount of preexisting EC particles, or

that photo-oxidation of VOCs was minimized due to lower solar radiation.

3.6 Evolutions of hygroscopicity and effective density with particle growth

As shown in Figure 5, three "banana-shaped" evolutions of the particle size distribution were identified in the representative PM episode. The banana-type contour plot of particle size distributions is a typical characteristics of new particle formation (NPF) events and traditionally regarded as one of the most important criteria for identifying NPF (Xiao et al., 2015;Dal Maso et al., 2005;Levy et al., 2013;Zhang et al., 2012). Atmospheric NPF is often defined by the burst of nucleation mode particles and subsequent growth of the nuclei to larger particles (Zhang et al., 2012;Kulmala et al., 2012). Gas-phase sulfuric acid produced via oxidation of SO_2 by OH radical plays a dominant role in the NPF events. NPF is typically completely suppressed when preexisting particles is abundant, because gas-phase sulfuric acid is rapidly lost to the surfaces of preexisting aerosols (Zhang et al., 2012). In addition to sulfuric acid, low-volatility organic species, and interaction between sulfate and organics are important for NPF (Zhang et al., 2004;Zhao et al., 2009). However, the possibility of NPF can be ignored in this study due to the absence of the burst of nucleation mode particles and the high concentration of $PM_{1.0}$. The burst of Aitken mode particles in the current study may be attributable to rapid accumulation of traffic emissions during rush hours under stagnant atmospheric conditions. The ''banana-shaped'' particle growth in the time evolution of particle size distribution from the Aitken mode size range to accumulation mode size range was primarily due to coagulation and condensation processes. This feature provided an excellent opportunity

to reveal the chemical mechanism of particle growth during the PM episode.

The first "banana-shaped" evolution of the particle size distribution occurred from approximately 05:00 to 15:00 on January 9, with increase of the particle number concentration (N_{total}) from 1.7×10^4 to 3.4×10^4 cm^{-3} followed by a decrease trend until 17:00 (Period 1). The second "banana-shaped" evolution occurred from approximately 18:00 on January 9 to approximately 12:00 on January 10 (Period 2). The N_{total} increased from 2.1×10^4 to 4.2×10^4 cm^{-3} within 3 h, followed by gradual decrease of N_{total} in contrast to a continuous increase of the particle mass concentration. During the growth process, the mode diameter of the particle population increased from below 40 nm to approximately 200 nm. The third "banana-shaped" evolution began in the evening rush hours on January 10, with the continuous increase of PM mass concentration for 12 h (Period 3). The latter two banana-shaped evolutions lasted long enough to tracer the changes in hygroscopicity and effective density due to particle growth.

Figure 8 illustrates the evolution of particle hygroscopicity and effective density during periods 2 and 3. During the initial stage, the measured GF and effective density distributions were both bimodal, with a dominant peak at GF = ~1.0 and ρ_{eff} = ~1.0 g cm^{-3}, respectively. In a previous study, we found that the number fraction of near-hydrophobic particles varied with the traffic exhaust (Ye et al., 2013). Moreover, laboratory studies showed that the effective density of 50 nm vehicle particles was approximately 1.0 g cm^{-3} (Olfert et al., 2007;Park et al., 2003;Momenimovahed and Olfert, 2015). These findings indicate that the initial burst of Aitken mode particles is attributable to the presence of enhanced traffic-related

emissions. In contrast, the number fraction and GF of the more-hygroscopic group increased with the growing particle size, indicating the addition of hygroscopic inorganic species. The variation of the effective density of the particles was similar to that of the hygroscopicity, indicating the increase of high density materials. In general, inorganic sulfate and nitrate are more hygroscopic and denser than soot particles or organic aerosols (Yin et al., 2015). These findings suggest that secondary sulfate and nitrate increased with the growing particle size, indicating the importance of the conversion of SO_2 and NO_x in particle growth. This conclusion is supported by the largest SNA concentration in $PM_{1.0}$ during the PM episode (31.3 μg m^{-3} on January 10 and 23.8 μg m^{-3} on January 11). Considering that the concentration of nitrate was much higher than that of sulfate during the haze event, the increase of hygroscopicity was dominated by the addition of nitrate.

4. Conclusions

Particle size distribution, size-resolved hygroscopic growth and effective density of sub-micrometer aerosols were determined using a HTDMA-APM system, along with measurements of cascade impactor samples and single particle mass spectrometry in urban Shanghai during winter 2014.

The PM episode exhibited a periodic cycle of ~5 days. The average concentration of $PM_{2.5}$ was 87 ± 67 μg m^{-3}, with approximately 62% of hourly $PM_{2.5}$ concentrations exceeding the Chinese Grade II guideline. Both secondary inorganic salts and carbonaceous aerosols contributed substantially to haze

formation, because the mass ratio of SNA/$PM_{1.0}$ fluctuated slightly around 0.28 during the observation period. Nitrate became the most abundant ionic species at $PM_{1.0}$ >40 μg m^{-3}, indicating that the sources of nitrate contributed more to haze formation in Shanghai than did SO_2.

The severe haze pollution was likely triggered by the adverse meteorological conditions, which favored the accumulation of local emissions and subsequent rapid growth to larger particles. As the PM episode developed, the number fraction of nearly-hydrophobic particles of different size increased, consistent with decrease of the mean effective density. Both hygroscopicity and effective density of the particles were found to increase considerably with growing particle size, indicating that secondary aerosol formation was one of the most important contributors to particle growth. Our results suggest that the accumulation of local emissions under adverse meteorological conditions and subsequent rapid particle growth by secondary processes are primarily responsible for the haze pollution in Shanghai during wintertime.

Acknowledgments

This work was supported by the National Natural Science Foundation of China (21477020, 21527814, and 91544224), and the National Science and Technology Support Program of China (2014BAC22B01).

Reference

Aggarwal, S. G., Mochida, M., Kitamori, Y., and Kawamura, K.: Chemical closure study on hygroscopic

properties of urban aerosol particles in Sapporo, Japan, Environmental Science & Technology, 41, 6920-6925, 10.1021/es063092m, 2007.
Chen, D., Liu, Z., Fast, J., and Ban, J.: Simulations of sulfate-nitrate-ammonium (SNA) aerosols during the extreme haze events over northern China in October 2014, Atmospheric Chemistry and Physics, 16, 10707-10724, 10.5194/acp-16-10707-2016, 2016.
Chu, B., Zhang, X., Liu, Y., He, H., Sun, Y., Jiang, J., Li, J., and Hao, J.: Synergetic formation of secondary inorganic and organic aerosol: effect of SO2 and NH3 on particle formation and growth, Atmospheric Chemistry and Physics, 16, 14219-14230, 10.5194/acp-16-14219-2016, 2016.
Dal Maso, M., Kulmala, M., Riipinen, I., Wagner, R., Hussein, T., Aalto, P. P., and Lehtinen, K. E. J.: Formation and growth of fresh atmospheric aerosols: eight years of aerosol size distribution data from SMEAR II, Hyytiala, Finland, Boreal Environment Research, 10, 323-336, 2005.
Dinar, E., Mentel, T. F., and Rudich, Y.: The density of humic acids and humic like substances (HULIS) from fresh and aged wood burning and pollution aerosol particles, Atmospheric Chemistry and Physics, 6, 5213-5224, 2006.
Fu, Q. Y., Zhuang, G. S., Wang, J., Xu, C., Huang, K., Li, J., Hou, B., Lu, T., and Streets, D. G.: Mechanism of formation of the heaviest pollution episode ever recorded in the Yangtze River Delta, China, Atmospheric Environment, 42, 2023-2036, 2008.
Gasparini, R., Li, R. J., Collins, D. R., Ferrare, R. A., and Brackett, V. G.: Application of aerosol hygroscopicity measured at the Atmospheric Radiation Measurement Program's Southern Great Plains site to examine composition and evolution, J. Geophys. Res.-Atmos., 111, D05S12, doi:10.1029/2004JD005448, 10.1029/2004jd005448, 2006.
Guan, W. J., Zheng, X. Y., Chung, K. F., and Zhong, N. S.: Impact of air pollution on the burden of chronic respiratory diseases in China: time for urgent action, Lancet, 388, 1939-1951, 2016.
Guo, S., Hu, M., Guo, Q., Zhang, X., Schauer, J. J., and Zhang, R.: Quantitative evaluation of emission controls on primary and secondary organic aerosol sources during Beijing 2008 Olympics, Atmospheric Chemistry and Physics, 13, 8303-8314, 10.5194/acp-13-8303-2013, 2013.
Guo, S., Hu, M., Zamora, M. L., Peng, J., Shang, D., Zheng, J., Du, Z., Wu, Z., Shao, M., Zeng, L., Molina, M. J., and Zhang, R.: Elucidating severe urban haze formation in China, Proceedings of the National Academy of Sciences of the United States of America, 111, 17373-17378, 10.1073/pnas.1419604111, 2014.
Gysel, M., Crosier, J., Topping, D. O., Whitehead, J. D., Bower, K. N., Cubison, M. J., Williams, P. I., Flynn, M. J., McFiggans, G. B., and Coe, H.: Closure study between chemical composition and hygroscopic growth of aerosol particles during TORCH2, Atmospheric Chemistry and Physics, 7, 6131-6144, 2007.
Gysel, M., McFiggans, G. B., and Coe, H.: Inversion of tandem differential mobility analyser (TDMA)

449 measurements, Journal of Aerosol Science, 40, 134-151, 10.1016/j.jaerosci.2008.07.013, 2009.
450 Han, B., Zhang, R., Yang, W., Bai, Z., Ma, Z., and Zhang, W.: Heavy haze episodes in Beijing during
451 January 2013: Inorganic ion chemistry and source analysis using highly time-resolved measurements
452 from an urban site, Science of The Total Environment, 544, 319-329,
453 http://dx.doi.org/10.1016/j.scitotenv.2015.10.053, 2016.
454 Heal, M. R., Kumar, P., and Harrison, R. M.: Particles, air quality, policy and health, Chemical Society
455 Reviews, 41, 6606-6630, 10.1039/c2cs35076a, 2012.
456 Hu, M., Peng, J., Sun, K., Yue, D., Guo, S., Wiedensohler, A., and Wu, Z.: Estimation of size-resolved
457 ambient particle density based on the measurement of aerosol number, mass, and chemical size
458 distributions in the winter in Beijing, Environ Sci Technol, 46, 9941-9947, 10.1021/es204073t, 2012.
459 Hu, Q. Q., Fu, H. B., Wang, Z. Z., Kong, L. D., Chen, M. D., and Chen, J. M.: The variation of
460 characteristics of individual particles during the haze evolution in the urban Shanghai atmosphere,
461 Atmospheric Research, 181, 95-105, 10.1016/j.atmosres.2016.06.016, 2016.
462 Huang, R.-J., Zhang, Y., Bozzetti, C., Ho, K.-F., Cao, J.-J., Han, Y., Daellenbach, K. R., Slowik, J. G.,
463 Platt, S. M., Canonaco, F., Zotter, P., Wolf, R., Pieber, S. M., Bruns, E. A., Crippa, M., Ciarelli, G.,
464 Piazzalunga, A., Schwikowski, M., Abbaszade, G., Schnelle-Kreis, J., Zimmermann, R., An, Z., Szidat,
465 S., Baltensperger, U., El Haddad, I., and Prevot, A. S. H.: High secondary aerosol contribution to
466 particulate pollution during haze events in China, Nature, 514, 218-222, 10.1038/nature13774, 2014.
467 IPCC: Climate Change 2013: The Physical Science Basis, Cambridge, UK, 2013.
468 Khalizov, A. F., Xue, H., Wang, L., Zheng, J., and Zhang, R.: Enhanced Light Absorption and Scattering
469 by Carbon Soot Aerosol Internally Mixed with Sulfuric Acid, Journal of Physical Chemistry A, 113,
470 1066-1074, 10.1021/jp807531n, 2009.
471 Kulmala, M., Petaja, T., Nieminen, T., Sipila, M., Manninen, H. E., Lehtipalo, K., Dal Maso, M., Aalto,
472 P. P., Junninen, H., Paasonen, P., Riipinen, I., Lehtinen, K. E., Laaksonen, A., and Kerminen, V. M.:
473 Measurement of the nucleation of atmospheric aerosol particles, Nature protocols, 7, 1651-1667,
474 10.1038/nprot.2012.091, 2012.
475 Levy, M. E., Zhang, R. Y., Khalizov, A. F., Zheng, J., Collins, D. R., Glen, C. R., Wang, Y., Yu, X. Y.,
476 Luke, W., Jayne, J. T., and Olaguer, E.: Measurements of submicron aerosols in Houston, Texas during
477 the 2009 SHARP field campaign, J. Geophys. Res.-Atmos., 118, 10518-10534, 10.1002/jgrd.50785, 2013.
478 Levy, M. E., Zhang, R. Y., Zheng, J., Tan, H. B., Wang, Y., Molina, L. T., Takahama, S., Russell, L. M.,
479 and Li, G. H.: Measurements of submicron aerosols at the California-Mexico border during the Cal-Mex
480 2010 field campaign, Atmospheric Environment, 88, 308-319, 10.1016/j.atmosenv.2013.08.062, 2014.
481 Li, J. J., Wang, G. H., Ren, Y. Q., Wang, J. Y., Wu, C., Han, Y. N., Zhang, L., Cheng, C. L., and Meng, J.
482 J.: Identification of chemical compositions and sources of atmospheric aerosols in Xi'an, inland China
483 during two types of haze events, Science of the Total Environment, 566, 230-237,

10.1016/j.scitotenv.2016.05.057, 2016.
Li, L., Huang, Z. X., Dong, J. G., Li, M., Gao, W., Nian, H. Q., Fu, Z., Zhang, G. H., Bi, X. H., Cheng, P., and Zhou, Z.: Real time bipolar time-of-flight mass spectrometer for analyzing single aerosol particles, International Journal of Mass Spectrometry, 303, 118-124, 10.1016/j.ijms.2011.01.017, 2011.
Li, P., Yan, R., Yu, S., Wang, S., Liu, W., and Bao, H.: Reinstate regional transport of $PM_{2.5}$ as a major cause of severe haze in Beijing, Proceedings of the National Academy of Sciences of the United States of America, 112, E2739-E2740, 10.1073/pnas.1502596112, 2015.
Lin, Y., Huang, K., Zhuang, G., Fu, J. S., Wang, Q., Liu, T., Deng, C., and Fu, Q.: A multi-year evolution of aerosol chemistry impacting visibility and haze formation over an Eastern Asia megacity, Shanghai, Atmospheric Environment, 92, 76-86, 10.1016/j.atmosenv.2014.04.007, 2014.
Liu, H. J., Zhao, C. S., Nekat, B., Ma, N., Wiedensohler, A., van Pinxteren, D., Spindler, G., Müller, K., and Herrmann, H.: Aerosol hygroscopicity derived from size-segregated chemical composition and its parameterization in the North China Plain, Atmospheric Chemistry and Physics, 14, 2525-2539, 10.5194/acp-14-2525-2014, 2014.
Malloy, Q. G. J., Nakao, S., Qi, L., Austin, R., Stothers, C., Hagino, H., and Cocker, D. R.: Real-Time Aerosol Density Determination Utilizing a Modified Scanning Mobility Particle SizerAerosol Particle Mass Analyzer System, Aerosol Science and Technology, 43, 673-678, 10.1080/02786820902832960, 2009.
Massling, A., Stock, M., Wehner, B., Wu, Z. J., Hu, M., Bruggemann, E., Gnauk, T., Herrmann, H., and Wiedensohler, A.: Size segregated water uptake of the urban submicrometer aerosol in Beijing, Atmospheric Environment, 43, 1578-1589, 2009.
Momenimovahed, A., and Olfert, J. S.: Effective density and volatility of particles emitted from gasoline direct injection vehicles and implications for particle mass measurement, Aerosol Sci. Technol., 49, 1051-1062, 10.1080/02786826.2015.1094181, 2015.
Niu, H. Y., Hu, W., Zhang, D. Z., Wu, Z. J., Guo, S., Pian, W., Cheng, W. J., and Hu, M.: Variations of fine particle physiochemical properties during a heavy haze episode in the winter of Beijing, Science of the Total Environment, 571, 103-109, 10.1016/j.scitotenv.2016.07.147, 2016.
Olfert, J. S., Symonds, J. P. R., and Collings, N.: The effective density and fractal dimension of particles emitted from a light-duty diesel vehicle with a diesel oxidation catalyst, Journal of Aerosol Science, 38, 69-82, 10.1016/j.jaerosci.2006.10.002, 2007.
Pagels, J., Khalizov, A. F., McMurry, P. H., and Zhang, R. Y.: Processing of Soot by Controlled Sulphuric Acid and Water CondensationMass and Mobility Relationship, Aerosol Sci. Technol., 43, 629-640, 10.1080/02786820902810685, 2009.
Park, K., F., C., Kittelson, D. B., and McMurry, P. H.: Relationship between particle mass and mobility for diesel exhaust particles Environmental Science and Technology, 37, 577-583, 2003.

519 Peng, J., Hu, M., Guo, S., Du, Z., Zheng, J., Shang, D., Zamora, M. L., Zeng, L., Shao, M., Wu, Y.-S.,
520 Zheng, J., Wang, Y., Glen, C. R., Collins, D. R., Molina, M. J., and Zhang, R.: Markedly enhanced
521 absorption and direct radiative forcing of black carbon under polluted urban environments, Proceedings
522 of the National Academy of Sciences of the United States of America, 113, 4266-4271,
523 10.1073/pnas.1602310113, 2016.
524 Petters, M. D., and Kreidenweis, S. M.: A single parameter representation of hygroscopic growth and
525 cloud condensation nucleus activity, Atmospheric Chemistry and Physics, 7, 1961-1971, 2007.
526 Qiao, T., Zhao, M., Xiu, G., and Yu, J.: Simultaneous monitoring and compositions analysis of PM_1 and
527 $PM_{2.5}$ in Shanghai: Implications for characterization of haze pollution and source apportionment, The
528 Science of the total environment, 557-558, 386-394, 10.1016/j.scitotenv.2016.03.095, 2016.
529 Rissler, J., Nordin, E. Z., Eriksson, A. C., Nilsson, P. T., Frosch, M., Sporre, M. K., Wierzbicka, A.,
530 Svenningsson, B., Londahl, J., Messing, M. E., Sjogren, S., Hemmingsen, J. G., Loft, S., Pagels, J. H.,
531 and Swietlicki, E.: Effective density and mixing state of aerosol particles in a near-traffic urban
532 environment, Environ Sci Technol, 48, 6300-6308, 10.1021/es5000353, 2014.
533 Shi, Y., Chen, J., Hu, D., Wang, L., Yang, X., and Wang, X.: Airborne submicron particulate (PM_1)
534 pollution in Shanghai, China: Chemical variability, formation/dissociation of associated semi-volatile
535 components and the impacts on visibility, Science of the Total Environment, 473, 199-206,
536 10.1016/j.scitotenv.2013.12.024, 2014.
537 Spencer, M. T., Shields, L. G., and Prather, K. A.: Simultaneous measurement of the effective density and
538 chemical composition of ambient aerosol particles, Environmental Science & Technology, 41, 1303-1309,
539 10.1021/es061425+, 2007.
540 Sun, Y. L., Chen, C., Zhang, Y. J., Xu, W. Q., Zhou, L. B., Cheng, X. L., Zheng, H. T., Ji, D. S., Li, J.,
541 Tang, X., Fu, P. Q., and Wang, Z. F.: Rapid formation and evolution of an extreme haze episode in
542 Northern China during winter 2015, Scientific Reports, 6, 10.1038/srep27151, 2016.
543 Swietlicki, E., Hansson, H. C., Hameri, K., Svenningsson, B., Massling, A., McFiggans, G., McMurry, P.
544 H., Petaja, T., Tunved, P., Gysel, M., Topping, D., Weingartner, E., Baltensperger, U., Rissler, J.,
545 Wiedensohler, A., and Kulmala, M.: Hygroscopic properties of submicrometer atmospheric aerosol
546 particles measured with H-TDMA instruments in various environments - a review, Tellus Ser. B-Chem.
547 Phys. Meteorol., 60, 432-469, 10.1111/j.1600-0889.2008.00350.x, 2008.
548 Tao, Y., Ye, X. N., Ma, Z., Xie, Y. Y., Wang, R. Y., Chen, J. M., Yang, X., and Jiang, S. Q.: Insights into
549 different nitrate formation mechanisms from seasonal variations of secondary inorganic aerosols in
550 Shanghai, Atmospheric Environment, 145, 1-9, 10.1016/j.atmosenv.2016.09.012, 2016.
551 Topping, D. O., McFiggans, G. B., and Coe, H.: A curved multi-component aerosol hygroscopicity model
552 framework: Part 1 - Inorganic compounds, Atmospheric Chemistry and Physics, 5, 1205-1222, 2005.
553 Turpin, B. J., and Lim, H. J.: Species contributions to PM2.5 mass concentrations: Revisiting common

554 assumptions for estimating organic mass, Aerosol Science and Technology, 35, 602-610,
555 10.1080/02786820152051454, 2001.
556 Wang, G., Zhang, R., Gomez, M. E., Yang, L., Zamora, M. L., Hu, M., Lin, Y., Peng, J., Guo, S., Meng,
557 J., Li, J., Cheng, C., Hu, T., Ren, Y., Wang, Y., Gao, J., Cao, J., An, Z., Zhou, W., Li, G., Wang, J., Tian,
558 P., Marrero-Ortiz, W., Secrest, J., Du, Z., Zheng, J., Shang, D., Zeng, L., Shao, M., Wang, W., Huang, Y.,
559 Wang, Y., Zhu, Y., Li, Y., Hu, J., Pan, B., Cai, L., Cheng, Y., Ji, Y., Zhang, F., Rosenfeld, D., Liss, P. S.,
560 Duce, R. A., Kolb, C. E., and Molina, M. J.: Persistent sulfate formation from London Fog to Chinese
561 haze, Proceedings of the National Academy of Sciences of the United States of America, 113, 13630-
562 13635, 10.1073/pnas.1616540113, 2016.
563 Wang, H., Xu, J., Zhang, M., Yang, Y., Shen, X., Wang, Y., Chen, D., and Guo, J.: A study of the
564 meteorological causes of a prolonged and severe haze episode in January 2013 over central-eastern China,
565 Atmospheric Environment, 98, 146-157, 10.1016/j.atmosenv.2014.08.053, 2014a.
566 Wang, Y., Wan, Q., Meng, W., Liao, F., Tan, H., and Zhang, R.: Long-term impacts of aerosols on
567 precipitation and lightning over the Pearl River Delta megacity area in China, Atmospheric Chemistry
568 and Physics, 11, 12421-12436, 10.5194/acp-11-12421-2011, 2011.
569 Wang, Y., Khalizov, A., Levy, M., and Zhang, R.: New Directions: Light absorbing aerosols and their
570 atmospheric impacts, Atmospheric Environment, 81, 713-715, 10.1016/j.atmosenv.2013.09.034, 2013.
571 Wang, Y., Zhang, Q., Jiang, J., Zhou, W., Wang, B., He, K., Duan, F., Zhang, Q., Philip, S., and Xie, Y.:
572 Enhanced sulfate formation during China's severe winter haze episode in January 2013 missing from
573 current models, J. Geophys. Res.-Atmos., 119, 10.1002/2013jd021426, 2014b.
574 Wang, Y., Zhang, R., and Saravanan, R.: Asian pollution climatically modulates mid-latitude cyclones
575 following hierarchical modelling and observational analysis, Nature Communications, 5,
576 10.1038/ncomms4098, 2014c.
577 Wang, Y. H., Liu, Z. R., Zhang, J. K., Hu, B., Ji, D. S., Yu, Y. C., and Wang, Y. S.: Aerosol
578 physicochemical properties and implications for visibility during an intense haze episode during winter
579 in Beijing, Atmospheric Chemistry and Physics, 15, 3205-3215, 10.5194/acp-15-3205-2015, 2015.
580 Wu, G., Li, Z., Fu, C., Zhang, X., Zhang, R., Zhang, R., Zhou, T., Li, J., Li, J., Zhou, D., Wu, L., Zhou,
581 L., He, B., and Huang, R.: Advances in studying interactions between aerosols and monsoon in China,
582 Science China-Earth Sciences, 59, 1-16, 10.1007/s11430-015-5198-z, 2016a.
583 Wu, S., Ni, Y., Li, H., Pan, L., Yang, D., Baccarelli, A. A., Deng, F., Chen, Y., Shima, M., and Guo, X.:
584 Short-term exposure to high ambient air pollution increases airway inflammation and respiratory
585 symptoms in chronic obstructive pulmonary disease patients in Beijing, China, Environment International,
586 94, 76-82, 10.1016/j.envint.2016.05.004, 2016b.
587 Wu, Z. J., Zheng, J., Shang, D. J., Du, Z. F., Wu, Y. S., Zeng, L. M., Wiedensohler, A., and Hu, M.: Particle
588 hygroscopicity and its link to chemical composition in the urban atmosphere of Beijing, China, during

summertime, Atmospheric Chemistry and Physics, 16, 1123-1138, 10.5194/acp-16-1123-2016, 2016c.
Xiao, S., Wang, Q. Y., Cao, J. J., Huang, R. J., Chen, W. D., Han, Y. M., Xu, H. M., Liu, S. X., Zhou, Y. Q., Wang, P., Zhang, J. Q., and Zhan, C. L.: Long-term trends in visibility and impacts of aerosol composition on visibility impairment in Baoji, China, Atmospheric Research, 149, 88-95, 10.1016/j.atmosres.2014.06.006, 2014.
Xiao, S., Wang, M. Y., Yao, L., Kulmala, M., Zhou, B., Yang, X., Chen, J. M., Wang, D. F., Fu, Q. Y., Worsnop, D. R., and Wang, L.: Strong atmospheric new particle formation in winter in urban Shanghai, China, Atmospheric Chemistry and Physics, 15, 1769-1781, 10.5194/acp-15-1769-2015, 2015.
Xie, Y., Ding, A., Nie, W., Mao, H., Qi, X., Huang, X., Xu, Z., Kerminen, V.-M., Petaja, T., Chi, X., Virkkula, A., Boy, M., Xue, L., Guo, J., Sun, J., Yang, X., Kulmala, M., and Fu, C.: Enhanced sulfate formation by nitrogen dioxide: Implications from in situ observations at the SORPES station, J. Geophys. Res.-Atmos., 120, 12679-12694, 10.1002/2015jd023607, 2015.
Yang, L., Zhou, X., Wang, Z., Zhou, Y., Cheng, S., Xu, P., Gao, X., Nie, W., Wang, X., and Wang, W.: Airborne fine particulate pollution in Jinan, China: Concentrations, chemical compositions and influence on visibility impairment, Atmospheric Environment, 55, 506-514, 10.1016/j.atmosenv.2012.02.029, 2012.
Ye, X. N., Chen, T. Y., Hu, D. W., Yang, X., Chen, J. M., Zhang, R. Y., Khakuziv, A. F., and Wang, L.: A multifunctional HTDMA system with a robust temperature control, Advances in Atmospheric Sciences, 26, 1235-1240, 10.1007/s00376-009-8134-3, 2009.
Ye, X. N., Ma, Z., Hu, D. W., Yang, X., and Chen, J. M.: Size-resolved hygroscopicity of submicrometer urban aerosols in Shanghai during wintertime, Atmospheric Research, 99, 353-364, 2010.
Ye, X. N., Ma, Z., Zhang, J. C., Du, H. H., Chen, J. M., Chen, H., Yang, X., Gao, W., and Geng, F. H.: Important role of ammonia on haze formation in Shanghai, Environ Res Lett, 6, Artn 024019
Doi 10.1088/1748-9326/6/2/024019, 2011.
Ye, X. N., Tang, C., Yin, Z., Chen, J. M., Ma, Z., Kong, L. D., Yang, X., Gao, W., and Geng, F. H.: Hygroscopic growth of urban aerosol particles during the 2009 Mirage-Shanghai Campaign, Atmospheric Environment, 64, 263-269, 10.1016/j.atmosenv.2012.09.064, 2013.
Yin, Z., Ye, X., Jiang, S., Tao, Y., Shi, Y., Yang, X., and Chen, J.: Size-resolved effective density of urban aerosols in Shanghai, Atmospheric Environment, 100, 133-140, 10.1016/j.atmosenv.2014.10.055, 2015.
Zhang, Q., Quan, J., Tie, X., Li, X., Liu, Q., Gao, Y., and Zhao, D.: Effects of meteorology and secondary particle formation on visibility during heavy haze events in Beijing, China, Science of The Total Environment, 502, 578-584, http://dx.doi.org/10.1016/j.scitotenv.2014.09.079, 2015a.
Zhang, R., Khalizov, A., Wang, L., Hu, M., and Xu, W.: Nucleation and Growth of Nanoparticles in the Atmosphere, Chemical Reviews, 112, 1957-2011, 10.1021/cr2001756, 2012.
Zhang, R., Guo, S., Zamora, M. L., and Hu, M.: Reply to Li et al.: Insufficient evidence for the contribution of regional transport to severe haze formation in Beijing, Proceedings of the National

624 Academy of Sciences of the United States of America, 112, E2741-E2741, 10.1073/pnas.1503855112,
625 2015b.
626 Zhang, R., Wang, G., Guo, S., Zarnora, M. L., Ying, Q., Lin, Y., Wang, W., Hu, M., and Wang, Y.:
627 Formation of Urban Fine Particulate Matter, Chemical Reviews, 115, 3803-3855,
628 10.1021/acs.chemrev.5b00067, 2015c.
629 Zhang, R. Y., Suh, I., Zhao, J., Zhang, D., Fortner, E. C., Tie, X. X., Molina, L. T., and Molina, M. J.:
630 Atmospheric new particle formation enhanced by organic acids, Science, 304, 1487-1490,
631 10.1126/science.1095139, 2004.
632 Zhang, R. Y., Khalizov, A. F., Pagels, J., Zhang, D., Xue, H. X., and McMurry, P. H.: Variability in
633 morphology, hygroscopicity, and optical properties of soot aerosols during atmospheric processing,
634 Proceedings of the National Academy of Sciences of the United States of America, 105, 10291-10296,
635 2008.
636 Zhao, J., Khalizov, A., Zhang, R., and McGraw, R.: Hydrogen-Bonding Interaction in Molecular
637 Complexes and Clusters of Aerosol Nucleation Precursors, Journal of Physical Chemistry A, 113, 680-
638 689, 10.1021/jp806693r, 2009.
639 Zhao, X. J., Zhao, P. S., Xu, J., Meng, W., Pu, W. W., Dong, F., He, D., and Shi, Q. F.: Analysis of a winter
640 regional haze event and its formation mechanism in the North China Plain, Atmospheric Chemistry and
641 Physics, 13, 5685-5696, 10.5194/acp-13-5685-2013, 2013.
642 Zheng, G. J., Duan, F. K., Su, H., Ma, Y. L., Cheng, Y., Zheng, B., Zhang, Q., Huang, T., Kimoto, T.,
643 Chang, D., Poeschl, U., Cheng, Y. F., and He, K. B.: Exploring the severe winter haze in Beijing: the
644 impact of synoptic weather, regional transport and heterogeneous reactions, Atmospheric Chemistry and
645 Physics, 15, 2969-2983, 10.5194/acp-15-2969-2015, 2015.

646

Figure and Table Captions

Figure 1 Schematic diagram of HTDMA-APM system.

Figure 2. Temporal evolutions of $PM_{1.0}$, $PM_{2.5}$, and PM_{10} concentrations during the winter observation.

Figure 3 Variations of sulfate, nitrate, and ammonium concentrations as a function of $PM_{1.0}$ mass loading.

Figure 4 Box plots showing hygroscopicity parameter and effective density at each dry diameter over the whole observation. The whiskers represent the 5^{th} and 95^{th} percentile, the two borders of box display the 25^{th} and 75^{th} percentile, and the band in each box denotes the median.

Figure 5 Temporal evolutions of particle number size distribution (A), volume size distribution (B), total number concentration and total volume concentration (C), and $PM_{1.0}$ concentration and calculated PM (less than 600 nm in mobility diameter) concentration during the representative PM episode from 7 to 12 January.

Figure 6 Evolutions of particle hygroscopic growth factor and effective density for different sizes during the representative PM episode.

Figure 7 Temporal evolutions of chemical compositions determined by SPAMS during the representative PM episode.

Figure 8 Particle hygroscopicity and density during the two particle growth processes

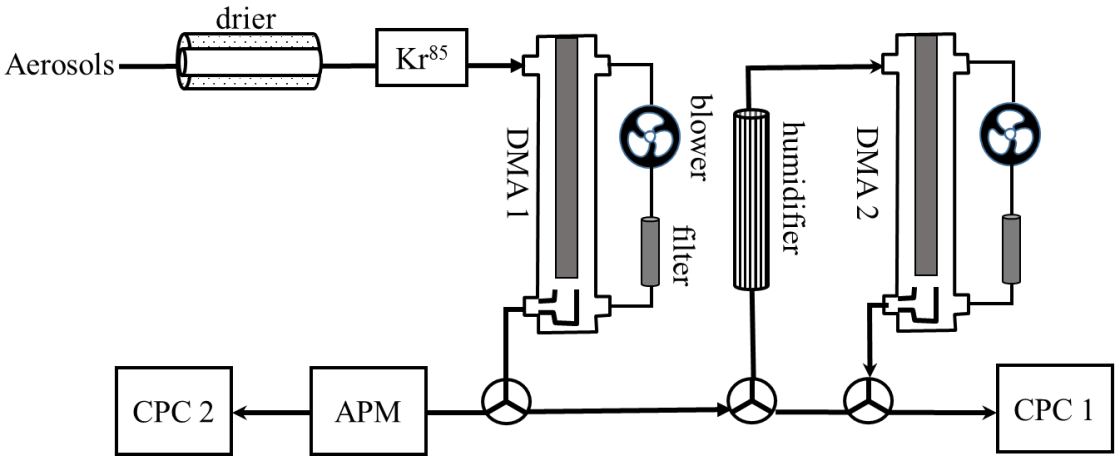

Figure 1 Schematic diagram of HTDMA-APM system.

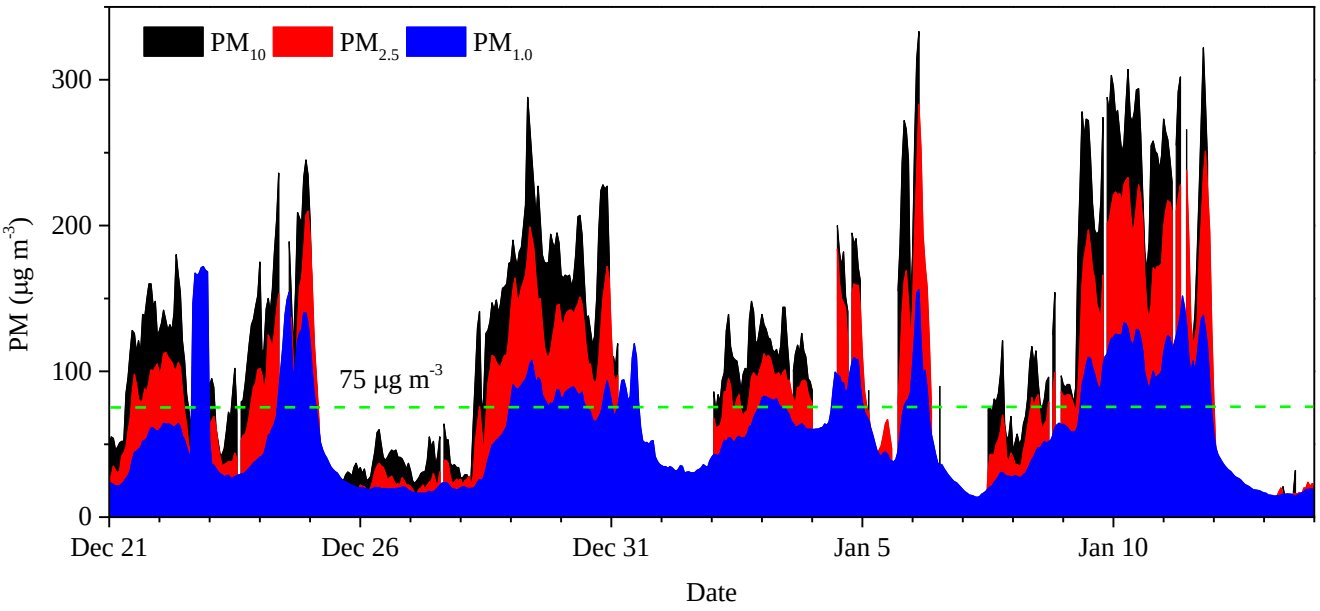

Figure 2. Temporal evolutions of $PM_{1.0}$, $PM_{2.5}$, and PM_{10} concentrations during the winter observation.

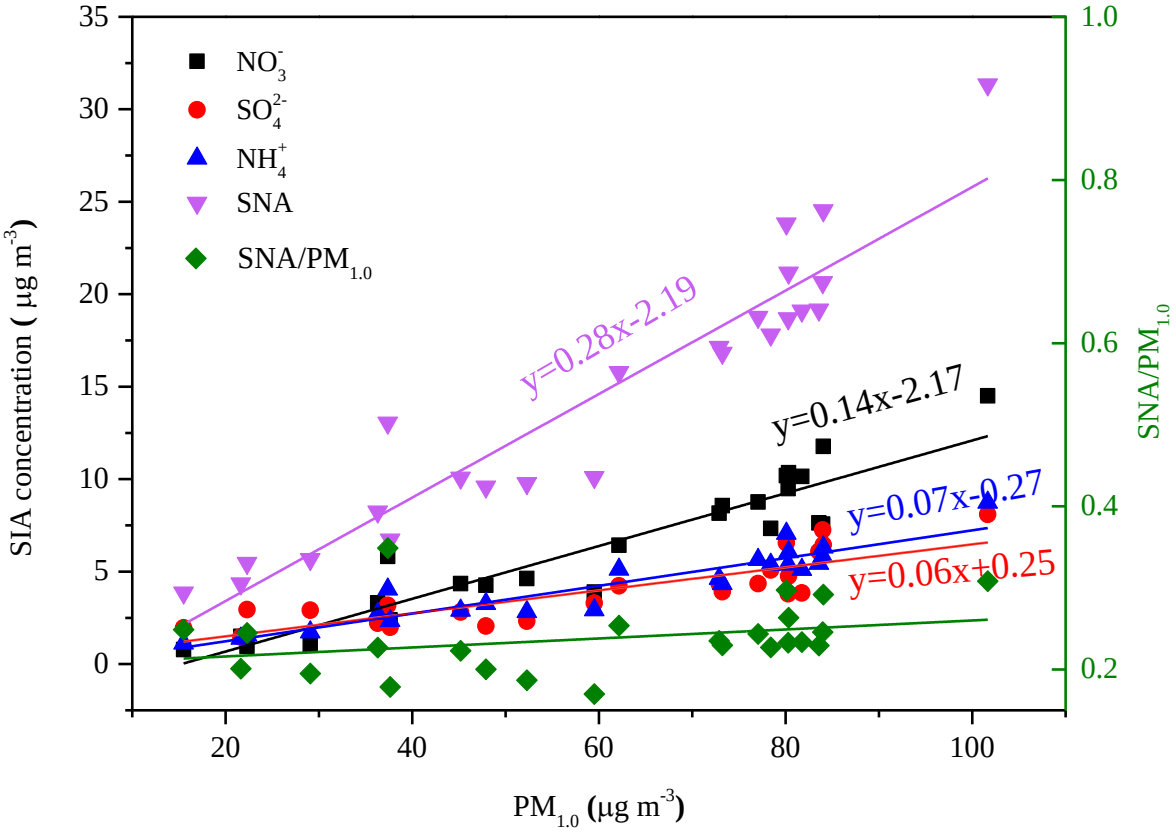

Figure 3 Variations of sulfate, nitrate, and ammonium concentrations as a function of $PM_{1.0}$ mass loading

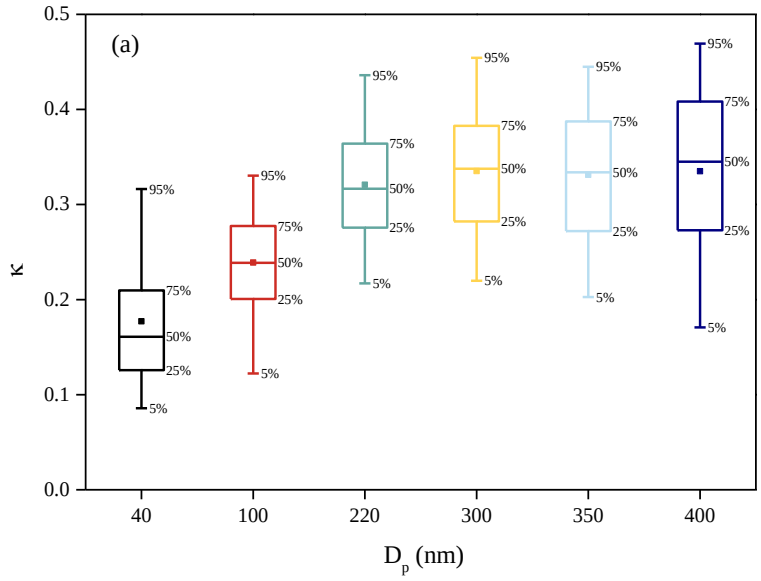

682

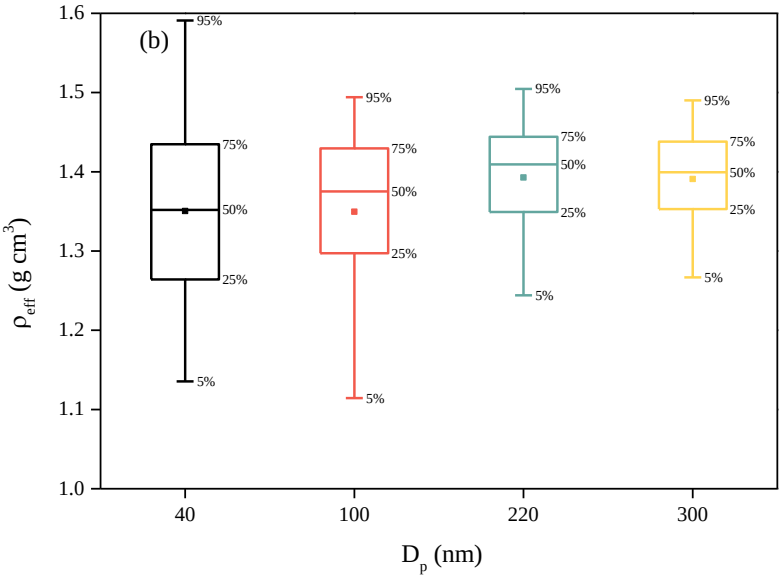

683

684 Figure 4 Box plots showing hygroscopicity parameter and effective density at each dry diameter over the
685 whole observation. The whiskers represent the 5th and 95th percentile, the two borders of box display the
686 25th and 75th percentile, and the band in each box denotes the median.

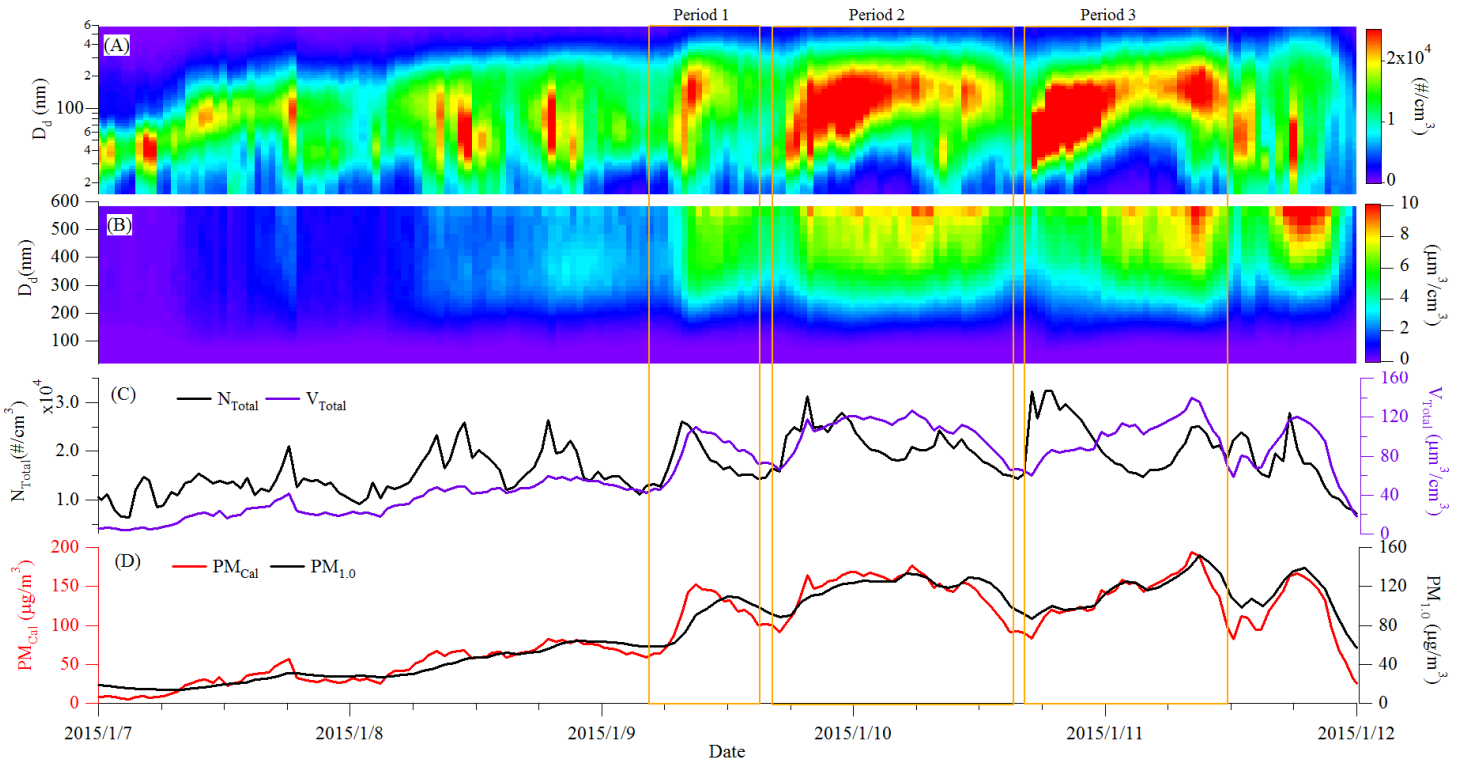

Figure 5 Temporal evolutions of particle number size distribution (A), volume size distribution (B), total number concentration and total volume concentration (C), and $PM_{1.0}$ concentration and calculated PM (less than 600 nm in mobility diameter) concentration during the representative PM episode from 7 to 12 January.

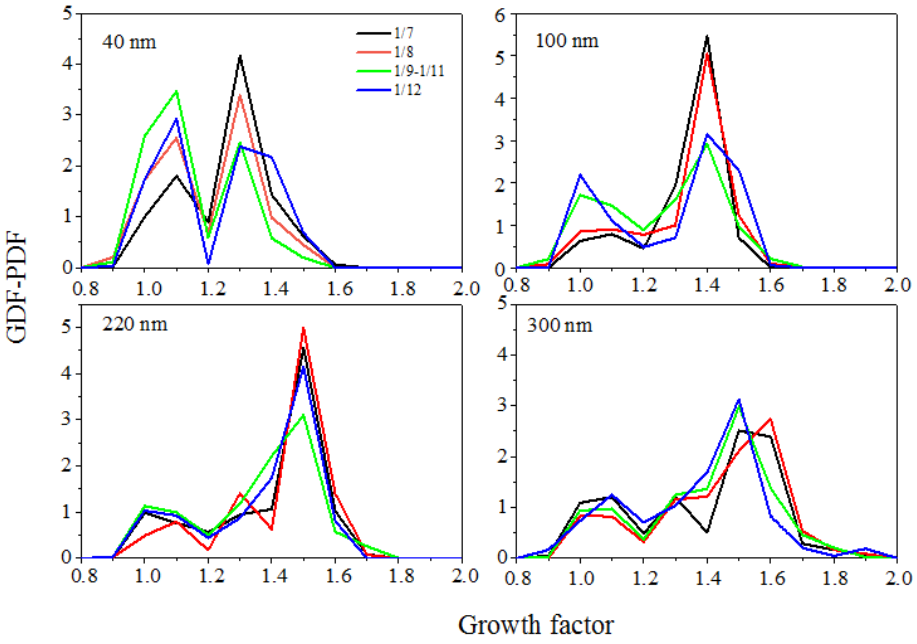

698

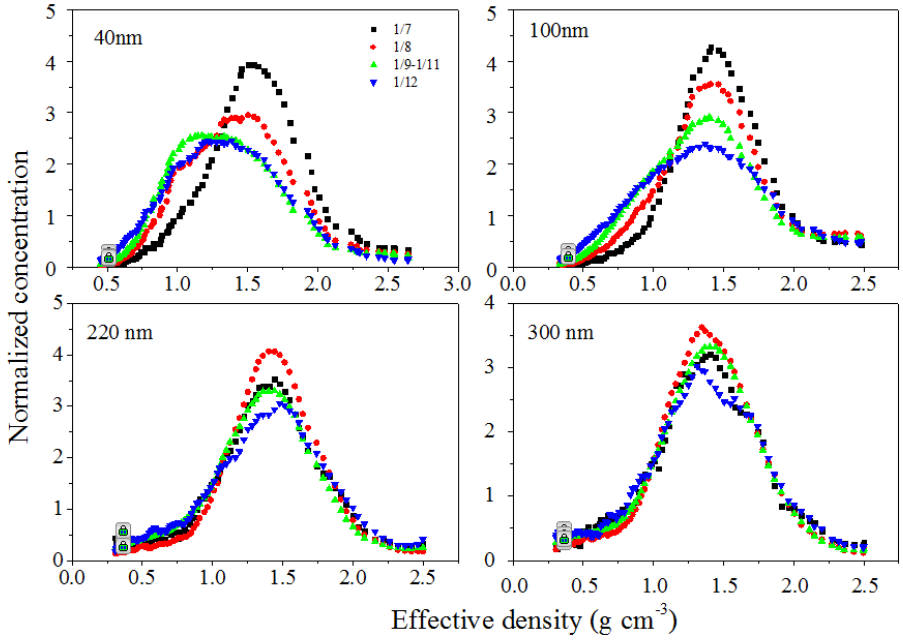

699

700 Figure 6 Evolutions of particle hygroscopic growth factor and effective density for different sizes during

701 the representative PM episode.

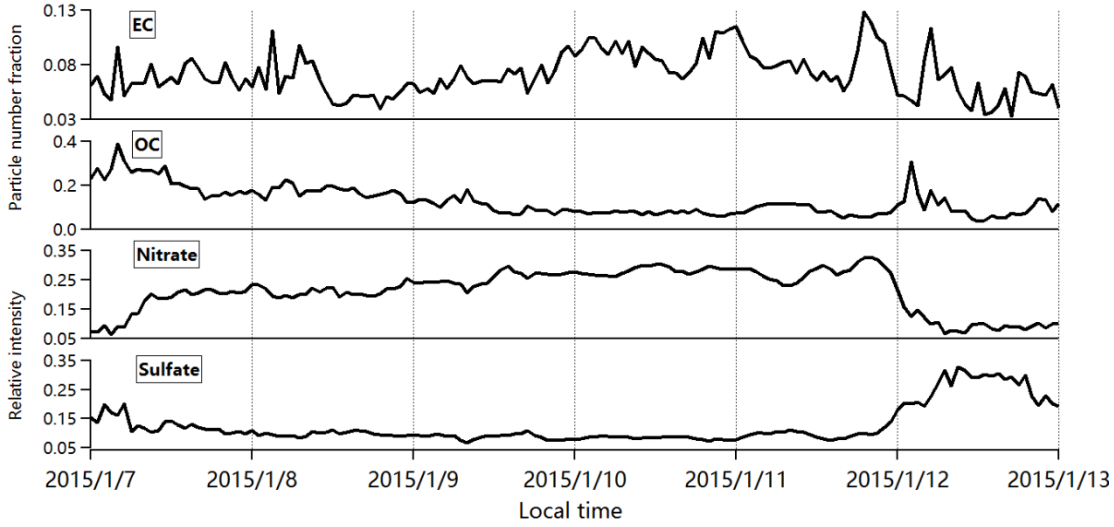

Figure 7 Temporal evolutions of chemical compositions determined by SPAMS during the representative PM episode.

709

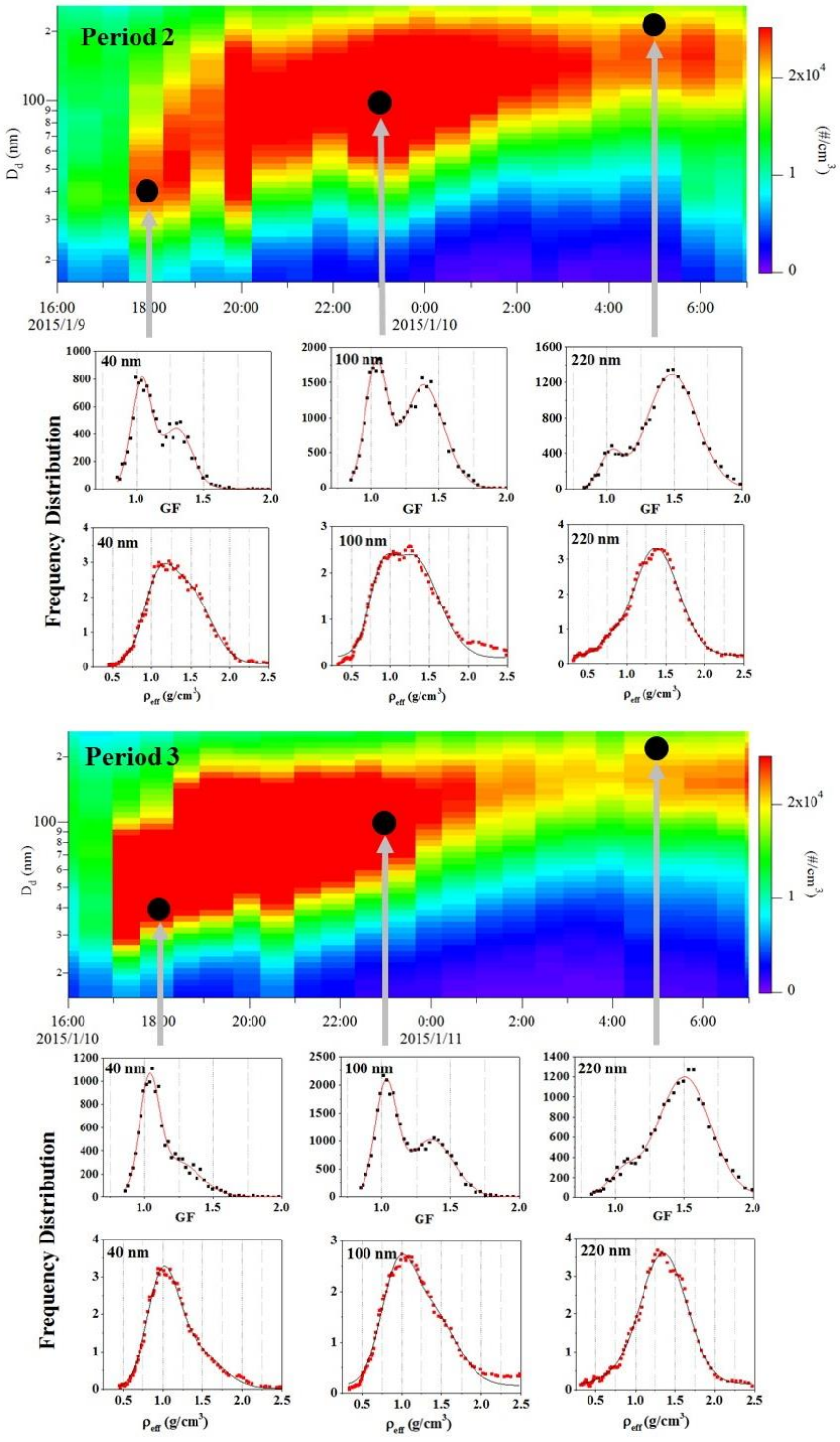

710

711 Figure 8 Particle hygroscopicity and density during the two particle growth processes.